Chemical Engineering Science 301 (2025) 120711

Contents lists available at ScienceDirect

Chemical Engineering Science

journal homepage: www.elsevier.com/locate/ces

Heterogeneous electro-Fenton oxidation of Congo red using carboxylic group activated carbon felt cathode: Electrokinetic mechanism and performance

Redae Nuguse Berhe [a,b], Monu Verma [a,e], Cong Li [c], Shimelis Kebede Kassahun [d], Joon Wun Kang [d], Hyunook Kim [a,*]

[a] Department of Environmental Engineering, University of Seoul, Seoul 02504, Republic of Korea
[b] Department of Chemical Engineering, Ethiopian Institute of Technology, Mekelle 0231, Ethiopia
[c] School of Environment and Architecture, University of Shanghai for Science and Technology, Shanghai 200093, China
[d] School of Chemical and Bio Engineering, Addis Ababa Institute of Technology, Addis Ababa University, Addis Ababa 1176, Ethiopia
[e] Department of Food Science and Technology, Graphic Era (Deemed to Be University), Dehradun, Uttarakhand, 248002, India

ARTICLE INFO

Keywords:
Carboxylic groups
Degradation efficiency
Heterogeneous catalyst
Oxygen-reduction reaction
Size-controlled MNPs

ABSTRACT

In this study, the carboxyl functional group (–COOH) saturated-carbon-felt (ACF) as functional cathode was prepared and used in heterogenous (Fe^{2+}) electro-Fenton (EF) catalytic degradation of Congo red (CR) in waster. As a heterogeneous catalyst, size-controlled magnetite (Fe_3O_4) nanoparticles (MNPs) were applied to the surface of the ACF cathode. The selectivity of ACF toward the two-electron oxygen-reduction reaction was estimated based on the proportion of H_2O_2 production; it was determined as >89 %. The removal efficiency of ACF for CR dye was 94 ± 2 % over 40 min reaction time, almost double that of a pristine CF cathode (48 ± 3 %). The kinetics data fitted to a pseudo-second order (PSO) model with K_2 of $8.8 \times 10^{-4} \pm 1.72 \times 10^{-5}$ mol^{-1} cm^3 min^{-1} (0.88 ± 0.02 M^{-1} min^{-1}). The mineralization current efficiency and TOC for CR were observed as 58 ± 2 %, and 83 ± 3 %, respectively. Overall, the results insight that the system could be a viable alternative method for treating dye-contaminated water.

1. Introduction

Large amounts of organic dyes and water are used in the textile industry. Direct discharge of wastewater by industry into natural water bodies can cause serious environmental pollution. If dyes were present in water, even at a very low concentration less than 1 mg L^{-1}, the penetration of sunlight into the water environment would be blocked and negatively affect the natural photo-degradation process. Since traditional biological treatment technologies are insufficient in degrading organic dyes in wastewater (Nakhate et al., 2020; Zuo et al., 2021), various technologies such as electro-coagulation, adsorption, membrane filtration, etc., have been employed to treat organic-dye-contaminated water. Since organic dyes are purposefully designed to resist being oxidized, treating them with traditional physiochemical and biological processes remains difficult (Chandanshive et al., 2020; Perecin et al., 2021).

Over the past a few decades, various advanced oxidation processes (AOPs) have been applied for degrading various organic dyes (Eq. (1)). The working principle of all AOPs is related to the generation of hydroxyl radical (•OH) (Hussain et al., 2020). The Fenton process, in which H_2O_2 reacts with Fe^{2+} to produce •OH continuously (Eq. (2)), is one of the most widely applied AOPs for degrading organic contaminants in wastewater. However, it requires a continuous supply of Fenton's reagents (H_2O_2 and Fe^{2+}) and a low working pH, while generating a large amount of iron-precipitate-containing sludge as a secondary contaminant (de Oliveira Guidolin et al., 2021).

$$\text{Organic contaminants} + \bullet OH \rightarrow \text{intermediates} \rightarrow CO_2 + 2H_2O \quad (1)$$

$$Fe^{2+} + H_2O_2 \rightarrow Fe^{3+} + OH^- + \bullet OH,\ E^0\ (\text{vs SHE}) = 2.80\ V \quad (2)$$

In current years, wastewater engineers have been engaged in the electro-Fenton (EF) process as an alternative to the traditional Fenton system. Since EF overcomes the drawbacks of the traditional Fenton process by *in situ* generating H_2O_2 and recycling electrons between Fe^{2+}

* Corresponding author.
E-mail address: h_kim@uos.ac.kr (H. Kim).

https://doi.org/10.1016/j.ces.2024.120711
Received 7 March 2024; Received in revised form 1 August 2024; Accepted 5 September 2024
Available online 10 September 2024

and Fe^{3+}, generates less sludge (Eq. (3)). Namely, H_2O_2 is continuously generated at cathode surface via two-electron oxygen-reduction reaction (2e-ORR) (Eq. (4)) and reduced to •OH radical by Fe^{2+} activation at the cathodic surface. Then, it commences to degrade nearby organic dyes (Li et al., 2021).

$$Fe^{3+} + e^- \rightarrow Fe^{2+},\ E^0\ (\text{vs SHE}) = 0.77\ \text{V} \quad (3)$$

$$O_2 + 2H^+ + 2e^- \rightarrow H_2O_2,\ E^0\ (\text{vs SHE}) = 0.547\ \text{V} \quad (4)$$

The H_2O_2 generation rate, which is limited by the low water solubility of O_2, limits in turn the whole EF process. As a result, gas diffusion electrodes have been employed to improve O_2 diffusion from the bulk solution to the electrode surface and to generate H_2O_2 on the cathodic surface (Hu et al., 2022). Among the factors affecting H_2O_2 generation in an EF process for degrading organic pollutants, selecting the right cathode material is the most essential. Due to its excellent electrolytic capacity, high electrochemical strength, and conductivity as well as biocompatibility, carbon electrodes (Huong Le et al., 2017; Zuo et al., 2021) and carbon felts (CFs) have been applied as cathode materials for EF processes (Qian et al., 2021; Yao et al., 2021). However, low wettability and electrochemical stability of CF have been an obstacle in wider CF applications (Xu et al., 2020). Therefore, many studies have been performed to chemically modify the surface of CF for improving its wettability and maintaining its electrochemical reactivity. For example, introducing oxygen-carrying functional groups such as carboxyl (–COOH), carbonyl (–C═O), and hydroxyl (–OH) groups into CF could significantly boost the interfacial surface electro-activity and wettability could enhance storage capacity and efficiency of a sodium-ion battery by improving the electrical activity and wettability of CF (Xu et al., 2023). Similarly, Kim et al. (2023) demonstrated that oxygen-containing functional groups could enhance electrolyte wettability and electrochemical performance of their activated CF (ACF). These functional groups also served as sites for H_2O_2 production, resulting in a greater rate of H_2O_2 generation.

Like conventional Fenton oxidation, EF oxidation requires a low working pH. As a result, heterogeneous EF oxidation based on the magnetite-nanoparticle (Fe_3O_4, MNP) catalyst has lately gained popularity in the treatment of organic dye wastewater because its working pH is wider than those of conventional EFs (Bello et al., 2019). In fact, insoluble MNPs have been shown to be an excellent heterogeneous alternative to water-soluble iron catalysts employed in homogeneous Fenton oxidation. Prominent attributes such as large surface area to volume ratio, good biocompatibility (Medina-ramírez et al., 2019), and ease of catalyst-recycling using an external magnet make MNPs a promising catalyst for degrading organic contaminants in wastewater (Hachemaoui et al., 2020).

In this study, an EF system was designed in which size-controlled-MNPs were employed as electron transfer channels between reacting solution and ACF cathodes for the degradation of Congo red (CR) dye, chosen as an organic pollutant model. The ACF was prepared by activating CF chemically to obtain oxygen-containing functional groups (such as –COOH, –C═O, and –OH), to remove inorganic contaminants and to increase the interfacial surface area and wettability of the ACF for electrochemical reduction of O_2. The role of MNP addition was investigated to pull H_2O_2 which was generated on the electro-active surface of the cathode to convert into •OH radicals. During experiments, various operating parameters such as the initial pH, applied potential, catalyst dose, and initial CR concentration were examined on the system performance. Lastly, the EF system was applied in treating real wastewater containing dye compounds and evaluated for its feasibility.

2. Materials and methods

2.1. Materials and chemical reagents

All chemical reagents used to synthesize the catalysts and electrodes were analytical grade and were used without further purification. Congo red (purity > 89 %), (Table S1), ethanol (>99 %), *para*-Benzoquinone (>98 %), *tert*-Butanol (>99.5 %), $FeSO_4{\cdot}7H_2O$ (>98 %), $Fe_2(SO_4)_3{\cdot}6H_2O$ (>99 %), Na_2SO_4 (>99 %), ammonia solution (28 wt%), stainless steel (SS; 6 cm × 2.5 cm; anode scientific-E160-0032), polyvinyl-cyanide-based CF (carbon content of >99 %; bulk density of 0.11–0.15 g cm^{-3}; tensile strength of 0.40 MPa) were purchased from Sigma-Aldrich (Seoul, Korea). All the solutions were made with ultrapure water with resistivity of more than 18 MΩ cm at 25 °C. During the experiment, 0.1 mol L^{-1} of H_2SO_4 and 0.1 mol L^{-1} of NaOH were used to adjust the initial pH of the solution.

2.2. MNPs synthesis and CF activation

Following the modified co-precipitation method described in Berhe et al. (2022) (Text S1), MNPs were synthesized using 6.87 g $Fe_2(SO_4)_3{\cdot}6H_2O$ and 4.73 g $FeSO_4{\cdot}7H_2O$ To activate pristine CF chemically, 12 cm^2 (4 cm × 3 cm) surface area of CF was soaked in the solution added with 0.75 mL of H_2SO_4 (5 wt%) and 1.75 mL of HNO_3 (5 wt%) for 30 min. Then, the material was soaked in DI water for 15 min, rinsed multiple times to produce ACF. Finally, the synthesized ACF was dried overnight at 105 °C in a drying oven to eliminate inorganic contaminants, if any, from the surface.

2.3. MNPs and ACF characterization

To estimate the crystalline size of the MNPs, powder X-ray diffraction (XRD, Rigaku, Tokyo, Japan) was used at 35 kV of energy and 40 mA of current with Cu K (λ = 1.541 Å) over the 2θ range of 5°–85° operating parameters. The oxygen-carrying functional groups on the surface of ACF were determined using Fourier transform infrared (FT-IR, Thermo Fisher Scientific, Nicolet iN10 mx, Seoul, Korea). The topological nature of the materials was studied using a field emission scanning electron microscope (FE-SEM, SU8010, Hitachi, Japan) at 15 kV. Energy Dispersive X-ray spectroscopy (EDX) was used to investigate the mapping and elemental composition of MNPs and ACF (Thermo Fisher Scientific Korea Ltd., Seoul, Korea).

X-ray photoelectron spectroscopy (XPS, Scienta-ESCA5500, Shimadzu, Kyoto, Japan) equipped with a high-resolution spectrometer (Horiba Scientific, Kyoto, Japan) was used for the ACF cathode analysis. A wide scan spectrum was obtained with binding energies ranging from 0 to 1400 eV and a pass energy of 185.75 eV. The C1s and O1s levels were measured with a step of 0.05 eV and a 12.75 eV pass energy. For data acquisition and data analysis, SCIENTA (Scienta Omicron, Lindome, Sweden) was used. The residual carbon C1s peak was employed to adjust the binding energy of each element (284.8 eV) (Greczynski and Hultman, 2020; Hu et al., 2022). A magnetic-property measurement system (MPMS-XL-7T, Quantum Design Inc., San Diego, CA, USA) was used to measure the magnetic characteristics of the MNPs (Boutemedjet et al., 2021). Cyclic voltammetry (CV, CHI660E, Chenhua, China) and linear sweep voltammetry (LSV) was used to measure current density ranging from −0.2 to +0.2 V (vs Ag/AgCl) at a scan rate of 10 mV s^{-1}. The synthesized cathodes were employed as a working electrode (1.2 cm × 0.96 cm), while Ag/AgCl (0.82 cm^2) and platinum plate (2.92 cm^2) were used as the reference electrode and the counter-electrode, respectively. The solution pH was adjusted to 4, and 0.5 mol L^{-1} of Na_2SO_4 was used as electrolyte. Using the Koutecky-Levich plot of the reciprocal square root of the angular velocity of the electrode vs the reciprocal limiting current (Eq. (5)); Hu et al., 2022), the average number of electrons transmitted (n) during ORR was calculated.

$$\frac{1}{i_L} = \left(\frac{1}{0.62\,n\,A\,F\,D^{2/3}C_i\,\nu^{-1/6}}\right)\omega^{-1/2} \quad (5)$$

where i_L is the limiting current (mA), n is the number of transferred electrons, F is the Faraday's constant (96,485.3 C mol^{-1}), D is the diffusion coefficient of O_2 (2.47×10^{-5} m^2 s^{-1}), A is the electrode area (1.2 cm × 0.96 cm), ν is the kinematic water viscosity (1×10^{-2} m^2 s^{-1}), C is the O_2 concentration at the electrode surface (1.67×10^{-6} mol L^{-1}), and ω is the rotation velocity (RPM) of the electrode.

2.4. Experimental and analytical methods

All the EF oxidation experiments were performed in a 500-mL cylindrical Pyrex reactor with a reaction volume of 300 mL. Initially, O_2 was supplied to the reactor solution at a rate of 300 mL min^{-1} for 10 min. Two stacks in the cathode–anode–cathode sequence (i.e., ACF-SS-ACF) with SS arranged in the middle were connected parallelly at 2.5 cm (Fig. 4). Water containing CR of 5–30 mg L^{-1} was treated under various operating conditions: pHs of 3–6, applied potentials of 0.5–6.5 V, and catalyst dosages of 0.1–0.6 g. Samples of 2 mL were harvested at every 5 min, and analyzed using UV–Vis spectrophotometer (Shimadzu 1900, Shimadzu, Kyoto, Japan) to determine the degradation efficiency (Menon et al., 2021) (Eq. (6)). In addition, total organic carbon (TOC) decay was analyzed using a TOC-V_{CPH} analyzer (Shimadzu, Kyoto, Japan) to determine the CR mineralization (Eq. (7)).

$$\text{CR removal}\,(\%) = \frac{C_0 - C_t}{C_0} \times 100 \quad (6)$$

$$\text{CR mineralization}\,(\%) = \frac{(TOC)_0 - (TOC)_t}{(TOC)_0} \times 100 \quad (7)$$

where C_0 and $(TOC)_o$ as well as C_t and $(TOC)_t$ are the CR concentration (mg L^{-1}) and TOC (mg C L^{-1}) before the CR oxidation and those after the oxidation, respectively.

Similarly, the electrochemical energy consumption (EEC, kWh g^{-1}) and mineralization current efficiency (MCE) were determined (Eqs. (8) and (9)), respectively (Ergan and Gengec, 2020).

$$EEC = \frac{1}{60}\frac{UjAt}{(TOC)_0 - (TOC)_t V} \quad (8)$$

$$MCE\,(\%) = 167 \times \frac{((TOC)_0 - (TOC)_t)nFV}{mjAt} \quad (9)$$

where U is cell voltage (V), n is the number of electrons transferred during CR oxidation (178e, Eq. (10)), assuming mineralization products would be NO_3^- and SO_4^{2-}, F is the Faraday's constant (96,485.3 C mol^{-1}), V is the solution volume (cm^{-3}), m is the carbon atoms in CR (32 atoms), j is the current density (mA cm^{-2}), A is the area of the electrode (cm^2), and t is the contact time (min).

$$[C_{32}H_{22}N_6O_6S_2]^{-2} + 84H_2O \rightarrow 32CO_2 + 6NO_3^- + 2SO_4^{2-} + 190H^+ + 178e^- \quad (10)$$

If the MNPs would not interact with the active species of ACF, and the space for CR degradation could occur only within the double layer, diffusion was considered as the only way of mass transport. Mathematically, the CR degradation rate was expressed as a function of •OH radical and CR concentration leading to a diffusional mass flux (Eq. (11)). The concentration of •OH radicals was assumed to be constant. The apparent rate constant (k_{app}) and the diffusion coefficient (D) were determined from Eq. (12).

$$\frac{dC_t}{dt} = -kC_{\bullet OH}C^*_t = -k_D\left(C^0_t - C^*_t\right), \text{ where } k_D = \frac{D}{\delta} \quad (11)$$

$$k_{app} = 16.67 \times \frac{nF}{jAV} \quad (12)$$

where C_t is the molar concentration of CR at any time t (mol L^{-1}), k is the second-order rate constant (mol^{-1} cm^3 min^{-1}), k_{app} is the pseudo-first-order rate constant (min^{-1}), $C_{\bullet OH}$ is the concentration of •OH radicals (mol L^{-1}), C^*_t is the concentration of CR at the electrode surface (mol L^{-1}), D is the diffusion coefficient of CR in water (1.95×10^{-6} cm^2 s^{-1}), δ is double-layer thickness (2.5×10^{-6} cm), n is the number of electrons transferred, A is the electrode area (2.5 cm × 3.5 cm), V is the reactor volume (300 cm^3), and C^0 is the initial CR concentration at the electrode surface (15 mg L^{-1} – 2.2×10^{-5} mol L^{-1}).

The residual iron content of the treated solution was quantified by inductively coupled plasma emission spectrometer (ICPE-900, Shimadzu, Kyoto, Japan). The chemical scavenging method was performed to determine the oxygen-reactive species involved in the CR oxidation (Guo et al., 2022). The intermediate products from the CR oxidation were analyzed by liquid chromatography-mass spectrometer (LC-MS, Shimadzu, Kyoto, Japan). In addition, the mineralized inorganic by-products (i.e., NO_3^- and SO_4^{2-} ions) were quantified by ion chromatography (IC; ICS-90, Thermo Fisher Scientific, Seoul, Korea). Before performing LC-MS and IC analysis, the samples were filtered through a 0.45-μm membrane filter (PTEF, ADVANTEC, Hp045an, Dublin, USA) (Zuo et al., 2021). To evaluate the capability of the process in treating real wastewater, wastewater was collected from the outlet of a secondary clarifier of a local wastewater treatment plant in Seoul, Korea. The wastewater sample was characterized (Table S2) and diluted ten times. To the diluted wastewater sample, proper amounts of CR, methylene blue (MB), and acid orange (AO) were added to make the concentration of each dye 5 mg L^{-1}. Then, the prepared wastewater was stored in a refrigerator until used. Each EF oxidation was performed for 120 min.

3. Results and discussion

3.1. Synthesis of size-controlled MNPs

Firstly, MNPs to be used in this study was synthesized by modifying with the classical co-precipitation method (Wu et al., 2011). In the beginning, HNO_3 was added (Eq. (13)) into ferric solution to form Fe $(OH)_3$. Separately, NaOH solution was carefully added (Eq. (15)) to ferrous solution to form $Fe(OH)_2$. When the two solutions were mixed, a black color precipitate could be observed as soon as reducing agent (20 mL NH_3 solution, 28 wt%) was added to the solution (Zanchettin, 2021) (Eq. (16)). A rod-shape magnet was used to remove the black precipitate from the solution for further investigation. The reactions forming different iron-water complexes, which are presented in Eqs. (13) through (16), are considered the key factors for size-distribution of MNPs (Liu et al., 2022; Menon et al., 2021).

$$[Fe(H_2O)_3(OH)_3]^+(aq) + H_3O^+ \rightleftharpoons Fe(OH)_3(s) + 3H_2O + 3H^+ \quad (13)$$

$$Fe(OH)_3(s) \rightarrow FeOOH(s) + H_2O \quad (14)$$

$$Fe^{2+} + 2OH^- \rightarrow Fe(OH)_2(s) \quad (15)$$

$$FeOOH + Fe(OH)_2 \rightarrow Fe_3O_4 + H_2O \quad (16)$$

3.2. Characterization of MNPs, CF, and ACF

The XRD technique was performed to determine the crystal size of MNPs and structures of ACF cathodes. Various diffraction peaks were obtained at 19.3°, 31.4°, 35.3°, 43.5°, 53.7°, 57.3°, 62.1° and 74.3°, which are corresponding to (1 1 1), (2 2 0), (3 1 1), (4 0 0), (4 2 2), (5 1 1), (4 4 0), and (6 2 2) lattice planes of MNPs, respectively (Fig. 1a); all the peaks were matched according to JCPDS No-19-0629 Standard (Cai et al., 2022). A higher diffraction peak was observed at 36.1° which is

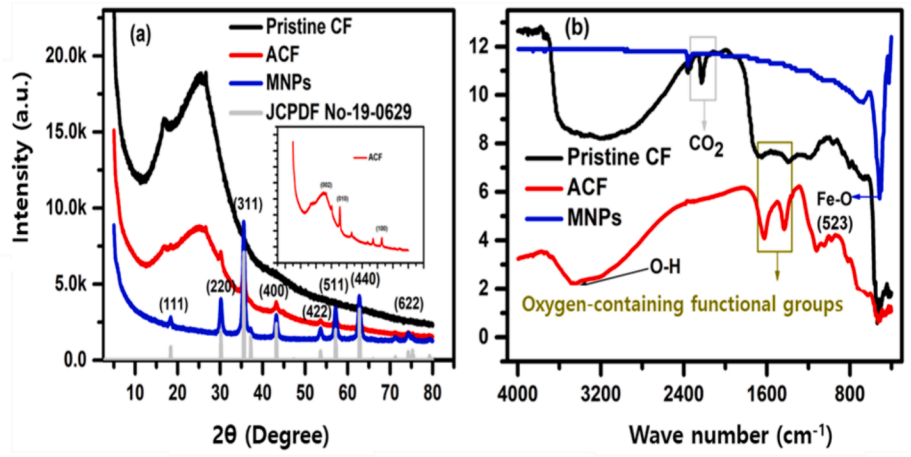

Fig. 1. XRD diffraction patterns (a) and FT-IR spectra (b). The insertion in (a) is ACF to show clear diffraction peaks.

attributed to the lattice plane of (3 1 1), and corresponding to it, the crystallite size and atomic layer distance within MNPs were calculated using Scherrer's and Bragg's laws (Text S2) (Jiang et al., 2021), and found to be 10.73 nm and 2.28 Å, respectively. The absence of any impurity peak, along with the peaks observed in Fig. 1a (blue), reveals the high purity of the synthesized MNPs crystal face of spinel structure (Liu et al., 2020). Higher anionic strength of SO_4^{2-} contributed to the formation of small-sizes MNPs (Jafari et al., 2021). The crystalline nature of pristine CF and ACF was also investigated. At around 17.5° and 26.9°, two large curved shapes were identified in pristine CF, which would pertain to the shapeless carbonization process of CF (Rahmani et al., 2021) (Fig. 1a, black). In the case of ACF, a tight peak was detected

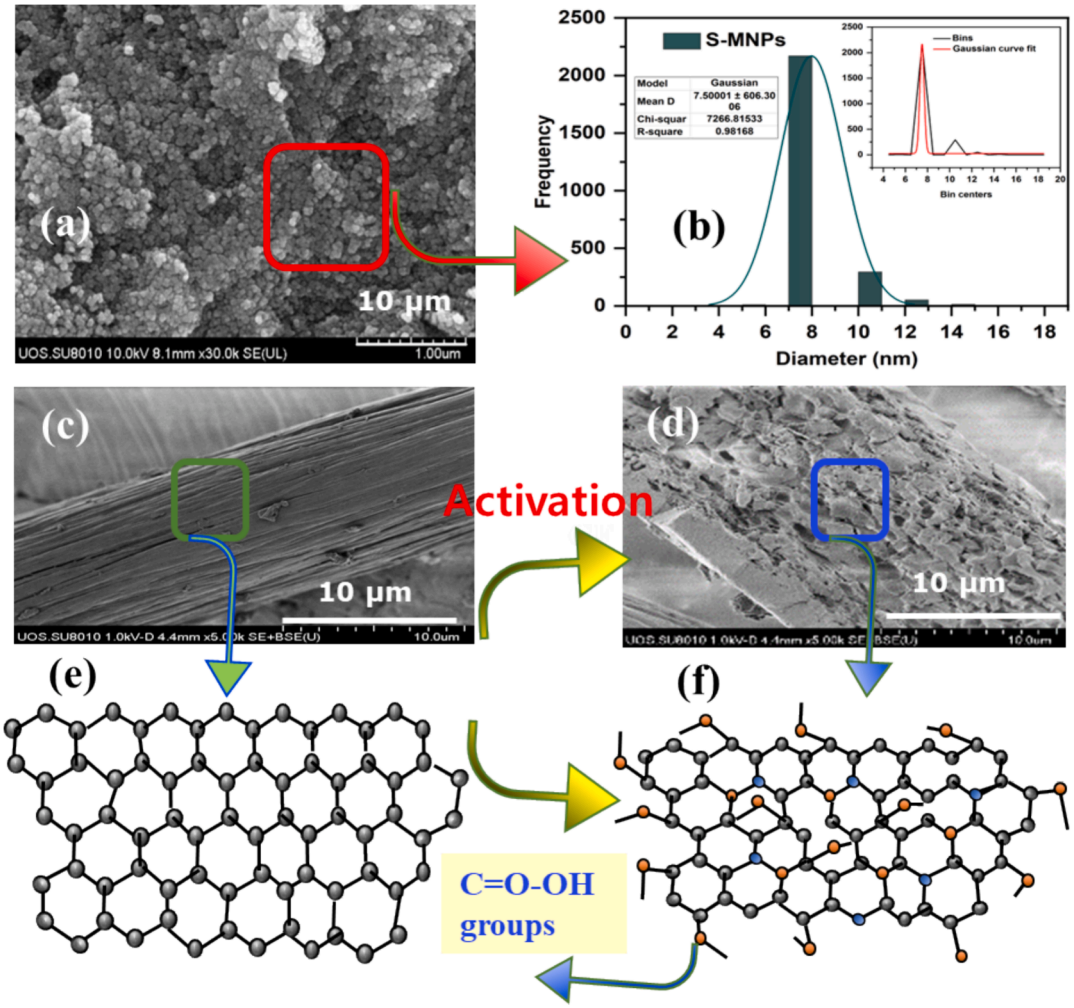

Fig. 2. Topographical structures of MNPs (a), pristine CF, and (c) ACF (d) in FE-SEM, and a plot of the MNPs size distribution (b). The structures in (e) and (f) defined the skeletal arrangement of carbon atoms in pristine CF and ACF, respectively.

at 2θ of 25° (0 0 2), which indicates the formation of the crystal structure of carbon (Fig. 1a, red, insert). Additional diffraction peaks observed at 2θs of 35.7° and 43.3° were attributed to the disordered graphite layer of amorphous carbon formed during the chemical treatment process (Jang et al., 2021). The additional diffraction peaks observed in ACF indicated that the CF was interracially activated, and oxygen-containing functional groups were formed.

Any functional group at the surface of MNPs and oxygen-containing functional groups formed during the CF activation were determined using FT-IR analysis. A strong peak at around 525 cm^{-1} was attributed to Fe-O bonds' stretching and vibrational modes; the vibration of the Fe-O is observed within 500–600 cm^{-1} (Mehdizadeh et al., 2021). The magnitude of the spectrum of MNPs that is drawn between 500 and 650 cm^{-1} would indicate the purity of the synthesized MNPs (Magro et al., 2020) (Fig. 1b, blue). In both CF and ACF, the peaks that were observed at about 2920 and 2241 cm^{-1}, were attributed to the symmetric and asymmetric vibration of –C–H and the bending vibration of adsorbed water (H–O–H), respectively. The peak at 1643 cm^{-1} was considered due to the –C═C stretching vibration. The peaks at approximately 1326 and 1164 cm^{-1} would be caused by the symmetrical bending vibration of C–H in pristine CF (Fig. 1b (black)). Moreover, small peaks were observed at around 1655 and 1554 cm^{-1} in ACF, which were assigned to stretching vibrations of carboxyl functional groups (–COOH) (Hassan and Tzedakis, 2020) and carbonyl functional groups (–C═O), respectively. The peaks at 1446 and 1246 cm^{-1} were considered mainly due to the –N–O groups and hydroxyl functional groups (–OH) (Kim et al., 2021), respectively (Fig. 1b, red). However, the peak at 2360 cm^{-1}, a characteristic one for the stretching vibration of CO_2, might be due to the adsorbed CO_2 during the sample preparation. The presence of new absorption peaks in ACF suggested that the material was successfully activated with oxygen-containing functional groups.

The topographical nature and structure of MNPs, CF, and ACF were determined by FESEM. The crystal size and structure of MNPs are displayed in Fig. 2a, and their mean diameter and their size distribution were determined using ImageJ software (Fiji is Just) (Cui et al., 2021) (Fig. 2b). An obvious difference was observed between the average crystallite size calculated by XRD (10.71 nm) and the average diameter calculated from FESEM images. It was clear that XRD analysis showed the crystallite size of MNPs not the size of the particles as a whole (Sheikhmohammadi et al., 2021); the difference was attributed to the agglomeration and magnetization of the particles during FESEM analysis. Since the particles possess high surface energy, they tend to aggregate to minimize the surface energy (Cui et al., 2021). Comparing the surface roughness of pristine CF (Fig. 2c) to that of ACF (Fig. 2d), rough walls of carbon fiber were observed in ACF. The formation of these scratched and rugged faces on the wall of the ACF was attributed to oxygen-containing functional groups on the ACF; these faces serve as a site for 2e-ORR. The chemical composition of the functional groups on the outer face wall of the pristine CF and ACF was determined as presented in Fig. 2e and f, respectively.

The EDX analysis was performed to determine the elemental composition of the synthesized materials (i.e., MNPs and ACF) as shown in Fig. S1. The clear and sharp peaks of Fe and O were observed from MNPs. Theoretically, the weight percent of O and Fe in 100 % pure Fe_3O_4 should be 27.6 % and 72.4 %, respectively. However, we found that those of our synthesized MNPs were 28.3 % and 71.7 %, indicating the purity was 99.1 % (Fig. S1a (Table)). In fact, other signals also could be observed from the MNPs, which was attributed to the impurities in the particles (Dash et al., 2019). Similarly, EDX and elemental mapping analysis were employed to further check the existence of other functional elements on the wall of ACF. Since pristine CF is an acrylonitrile compound, soaking it in a mixed H_2SO_4 and HNO_3 solution can change the surface chemistry of the material. As shown in Fig. S1b (1–6), the ACF cathode was found to contain carbon, oxygen, nitrogen, and sulfur elements in a uniform elemental distribution (Fig. S1b, Table).

To further confirm the formation of oxygen-carrying functional groups, i.e., carboxyl, carbonyl, nitro, and hydroxyl ones via activation of pristine CF, XPS studies were performed. The effect of the wet activation on pristine CF determines the surface chemistry and activity of the ACF cathode. The C1s and O1s spectral peaks of both pristine CF and ACF occurred at around 285 and 530 eV, respectively (Fig. 3). The spectral peaks for the pristine CF were considered due to the surface modification of the carbon structure and heteroatom molecules of oxygen which was attributed to the intrinsic water adsorbed to pristine CF (Greczynski and Hultman, 2020) as depicted in Fig. 3a. However, as demonstrated in Fig. 3b, high resolution spectra of C1s that were observed for the surface of ACF at the binding energies of 286.2, 284.8, and 283.9 eV were matched to carbonyl (–C═O) or hydroxyl (–OH), carboxyl (–COOH), and nitro (–N–O) functional groups, respectively (Hong et al., 2021; Hu et al., 2022). These oxygen-carrying functional groups indicated that the pristine CF was successfully activated. Furthermore, O1s peaks of pristine CF at 532.5 and 529.9 eV correspond to C–O species (Fig. 3c). To analyze the changes of C–O species after the activation of pristine CF, however, a comprehensive deconvolution of the peaks at 533.2, 531.1, and 530.3 eV was carried out (Fig. 3d). These peak-binding-energy positions correspond to N–C═O, –COOH and –C═O, respectively, which suggests the formation of active oxygen-carrying functional groups (Hong et al., 2021). Generally, the FT-IR, EDX spectra, and XPS data indicated pristine CF was successfully activated, and the oxygen-carrying functional groups were formed on the surface of CF without significant structural changes. The N1s spectral peak of ACF located at around 400.5 eV attributed to sp^2-hybrid N atoms of –C═N–C (Greczynski and Hultman, 2020; Hu et al., 2022) (Fig. S2). The N1s signal of ACF originated from pristine CF and the activation process did not change the chemical position of the N atom (Hu et al., 2022).

Using a VSM device, the magnetic properties of MNPs were measured at room temperature within the sweeping field ranging between −7.95 k and 7.95 k Oe. The hysteresis curve in Fig. 4a indicated that the synthesized MNPs exhibited ferromagnetic characteristics with magnetization saturation (M_S) of 74 emu/g, which was in accordance with Gang et al. (2021). Since the M_S value is dependent on the phase composition, crystallinity, and size of the synthesized particles (Boutemedjet et al., 2021), MNPs with a larger size would present a higher M_S value than smaller MNPs (Perecin et al., 2021). The observed VSM result for the synthesized MNPs confirmed that they could be easily separated from the aqueous medium using an external magnet after their use, e.g., in CR oxidation.

The electrochemical functionality of CF and ACF were tested using an electrochemical workstation to determine the electrochemical performance of both CF and ACF cathodes in a three-rotating-disk electrode system in O_2-saturated solution at 300-RPM angular speed. As described in Fig. 4b, the electrochemical property of the ACF electrode showed higher peak current densities in both oxidation (higher positive value, 6.79 ± 0.17 mA cm^{-2}) and reduction (higher negative value, −5.96 ± 0.14 mA cm^{-2}) than that of the pristine CF electrode, which could be attributed to porous surface-chemistry modification of the ACF (Greczynski and Hultman, 2020; Hu et al., 2022). Specifically, the oxygen-containing functional groups such as –COOH available on the surface would serve as a site for ORR and contribute to the higher current density. The higher current density of ACF indicated the better performance of ACF in electrochemical activity of the system, compared to that of pristine CF. To check ORR indirectly, the electrochemical analysis was repeated under N_2-saturated solution. Thus, a very limited magnitude of current density (approximately ± 0.15 mA cm^{-2}) was observed as described in Fig. S3a. The molecular ORR expression in O_2-saturated solution and ORR suppression in N_2-saturated solution confirmed the catalytic activity of ACF. The higher ORR catalytic performance of ACF in O_2-saturated solution was attributed to the high surface area to volume ratio of ACF; the high surface area in turn acted as a reservoir for H_2O_2 generation.

During the ORR mechanism, both convective-limiting and diffusive-

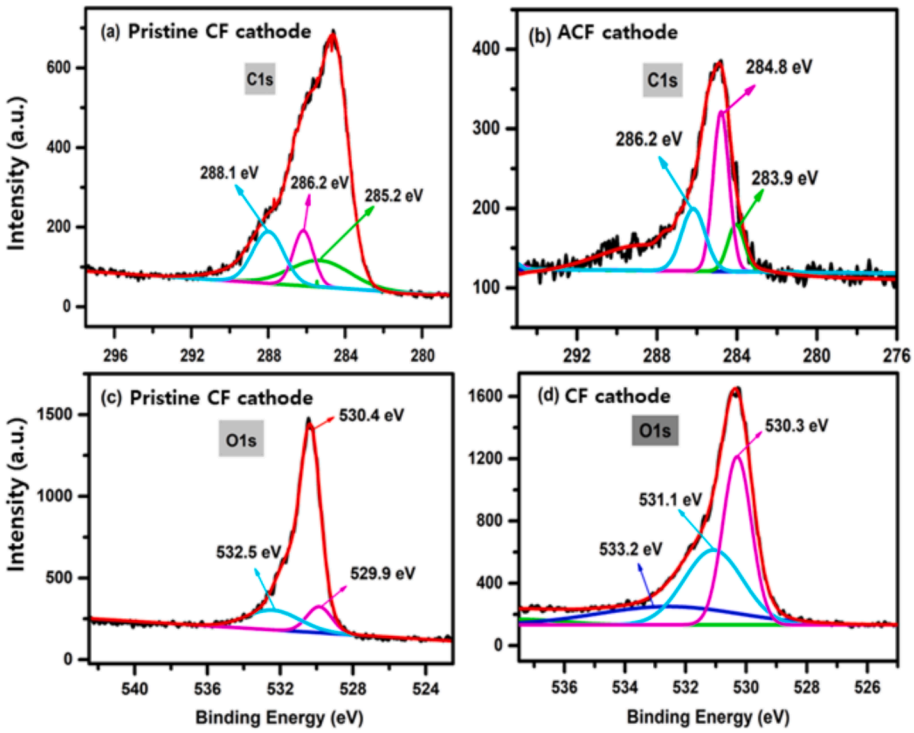

Fig. 3. High-resolution XPS measurement with curve fittings: (a) corresponds to C1s in pristine CF-cathode and (b) corresponds to C1s in ACF-cathode. On the Other hand (c) corresponds to O1s in pristine CF-cathode and (d) corresponds to ACF-cathode.

limiting currents were affected by the angular speed and could be determined using a Koutecky-Levich plot (Xia et al., 2019). The angular speed contributed to a smaller diffusion layer and a lower concentration gradient of electroactive species at the ACF surface. The sigmoidal curve in Fig. 4c explains the dependence of limiting current density on angular speed when the current density was solely controlled by mass transport (i.e., steady-state condition of active species on ACF). The limiting current density is directly related to the angular speed of the disk. The Koutecky-Levich plot (Fig. 4d; Eq. (5)) describes the kinetic contribution of electroactive species on ACF, which is used to determine the number of electrons transferred (n). Taking the Faraday's constant (F, 96,485.3 C mol^{-1}), diffusion coefficient of oxygen (D, 2.47 $\times$ 10^{-5} m^2 s^{-1}), electrode area (A, 1.2 cm $\times$ 0.96 cm), kinematic viscosity of water (v, 1 $\times$ 10^{-2} m^2 s^{-1}), concentration of oxygen at the electrode surface (C, 1.67 $\times$ 10^{-9} mol L^{-1}), and rotation speed (ω, RPM) at −0.15 V of cell potential, the number of electrons transferred were estimated to be 2.1 $\pm$ 0.01 (Gao et al., 2021; Hu et al., 2022). The number of transferred electrons (2.1 $\pm$ 0.01 e) during the ORR mechanism confirmed the selectivity of ACF toward 2e-ORR. The number of transferred electrons could be determined at various potentials (−0.2 to +0.2 V) using the slope of the Koutecky-Levich plot (Fig. 4e). The 2e-ORR reaction efficiency could be measured directly by the percent concentration of H_2O_2 generated at the surface of ACF (Zhang et al., 2022). The H_2O_2 produced at different cell potentials (−0.2 to +0.2 V) was plotted as described in Fig. 4f, and about 89 $\pm$ 3 % H_2O_2 generation was estimated according to Eq. (17) (Hu et al., 2022).

$$H_2O_2(\%)\ \text{generation} = 200 \times \frac{i_R}{Ni_D + i_R} \tag{17}$$

where N is the electron collection efficiency of the rotating disk and ring (0.27, equipment specification), which is the ratio of current in the ring to current in the disk, and i_R and i_D are the values of the ring and disk current densities at different cell potentials (−0.2 to +0.2 V).

The LSV analysis of pristine CF and ACF in O_2-saturated solution was performed as presented in Fig. S3b. The current response of the pristine CF cathode (3.75 $\pm$ 0.54 mA cm^{-2}) was less than that of ACF (more than 10 mA cm^{-2}). The result confirmed that the electrochemical catalytic activity of ACF was due to the contribution of surface modification (Qian et al., 2021). Again, the higher ORR in ACF was attributed to the oxygen-containing functional groups formed during the activation process, which was supported by the FTIR and XPS spectra results.

3.3. EF oxidation analysis

The degradation performance of ACF as a cathode was compared with that of pristine CF; in both cases, a stainless-steel (SS) electrode was used as an anode. The SS anode could facilitate to dissolve MNPs as heterogeneous Fe^{2+} catalyst in the solution and enhance the oxidation rate. To the reactor, CR of 10 mg L^{-1} was added along with 0.2-g heterogeneous catalyst (MNPs). Then, the solution pH was adjusted to 3.0 and the potential of 4.5 V was applied. The EF catalytic degradation efficiency of the prepared cathodes for CR degradation was determined based on the change of the maximum absorbance at 500 nm (Fig. 5). The height of absorption peak for CR continuously decreased over the reaction time, and finally disappeared after 40 min (Menon et al., 2021). Fig. 5a shows the catalytic (with MNPs) and non-catalytic (without MNPs) degradation of CR using the cathodes (pristine CF and ACF). Over 40-min EF reaction time, the CR removal efficiency of non-catalyst, pristine CF, and ACF reactions were 16 $\pm$ 2 %, 48 $\pm$ 3 %, and 94 $\pm$ 2 %, respectively. Fig. 5b and 5d show the EF stack cell before and after the CR degradation. The Cr-removal efficiency of ACF was two times higher than that of pristine CF and six times than that of non-catalyst as described in Fig. 5c.

The higher degradation efficiency of the ACF cathode could be due to its functional groups on its surface. These oxygen-containing active species facilitate easy transfer of electrons from and to the cathode surface (Xing et al., 2020). The easy transfer of electrons from and to the active cathode surface led to higher generation of current density. Similarly, changing the surface chemistry of the material contributes to the wettability issues that triggers rapid diffusion of DO to the cathode

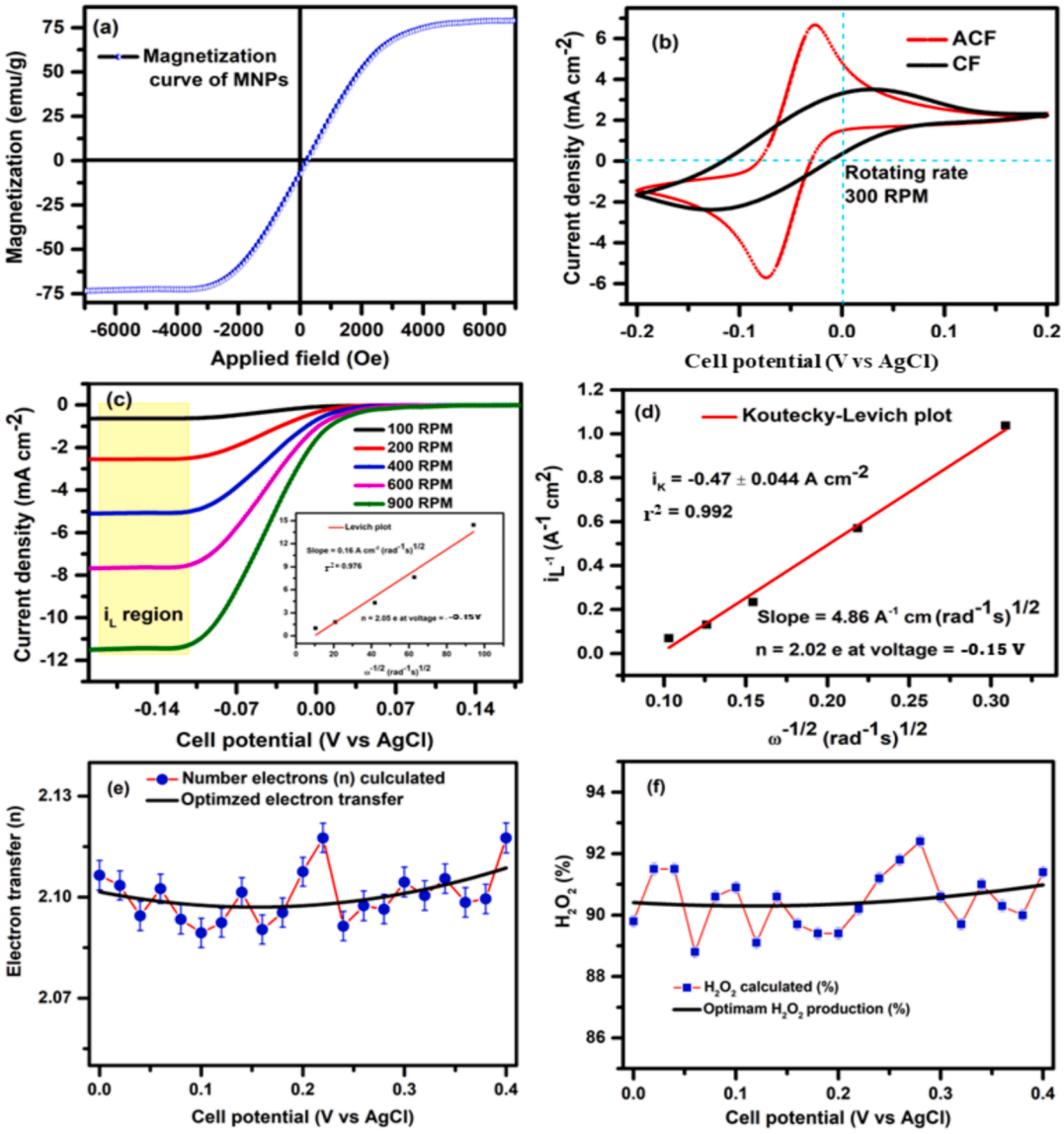

Fig. 4. Magnetization property (a), cyclic voltammetry (CV) (b), effect of rotating speed of the electrode on ACF (c), Koutecky-Levich plot (d), number of electrons transferred (e), and estimation of percentage H_2O_2 production (f). The scan rate was 10 mV s^{-1}, potential scan was −0.2 to + 02 V, the working pH was 4 and the used electrolyte was Na_2SO_4 (0.5 mol L^{-1}).

surface which facilitated 2e-ORR for H_2O_2 generation (Chen et al., 2021). However, the hydrophilicity of the cathode material could lower the generation of H_2O_2. Depending on the morphology of the MNPs on the CF or ACF electrode, the EF process showed different performance in CR degradation. In fact, the CR degradation relied on the particle size and iron content of MNPs. The iron content of MNPs is directly related to the amount of Fe^{2+} released into bulk solution, bringing about homogenous EF oxidation, which would subsequently produce higher H_2O_2 on the surface of the ACF.

3.4. Effects of operational parameters on CR degradation

The pH of the reaction medium is the main factor for Fenton's reaction and recycling of Fe^{3+}/Fe^{2+} during EF oxidation. In fact, lower removal efficiency is expected at more acidic conditions (pH < 3). Fe^{3+} could form an iron-water complex ($[Fe(H_2O)_6]^{3+}$) which could be hydrolyzed to $[Fe(H_2O)_5(OH)]^{2+}$. The presence of $[Fe(H_2O)_6]^{3+}$ and $[Fe(H_2O)_5(OH)]^{2+}$ could hinder recycling of Fe^{3+}/ Fe^{3+} to react with H_2O_2. In addition, H_2O_2 could be surrounded by protons to produce oxonium ions which are stable molecule that could prevent or reduce the activity of H_2O_2 toward Fe^{2+}, which in turn would blocks the generation of •OH radicals (Berhe et al., 2023; Hussain et al., 2020).

The highest catalytic degradation of CR (95 ± 3 %) was observed at acidic medium (≈ pH 3). The removal efficiency dropped to 70 ± 3 % when the pH value was adjusted to 6. Interestingly, 94 ± 3 % removal efficiency was achieved at pH 4 (Fig. 6a). However, at pH value higher than 4, auto-decomposition of H_2O_2 and formation of iron precipitates occurred, eventually leading to excessive sludge generation. These results were also reported by Sheikhmohammadi et al. (2021). After comparing the CR-removal efficiency of the EF oxidation at pH 3 and that at pH 4 and considering the associated chemical cost for pH adjustment, pH 4 was adopted for further experiment.

The driving factor for electron transfer within the bulk solution and the electrodes is the applied voltage (Gao et al., 2020), which eventually determines the performance of the EF oxidation process. In this case, the dependence of CR oxidation on applied voltage was determined by varying the voltage from 0.5 to 6.5 V. As the applied potential step-up from 0.5 to 3 V, the CR removal rate also sharply improved from 76 ± 2 % to 96 ± 3 % (Fig. 6b). It was hypothesized that application of a higher voltage would enhance the generation of H_2O_2 and the electron

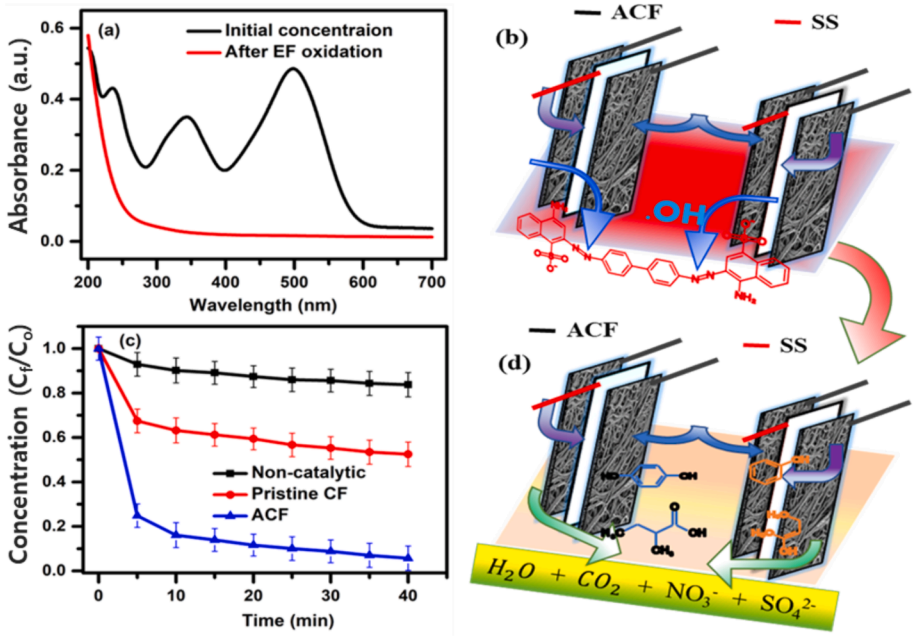

Fig. 5. Spectroscopic analysis before and after CR degradation (a), degradation kinetics (c), cell-configurations before (b) and after EF oxidation (d). Operating conditions: pH 3, applied potential of 4.5 V, catalyst dose of 0.2 g, initial CR concentration of 10 mg L^{-1}, and Na_2SO_4 of 0.5 mol L^{-1} as electrolyte.

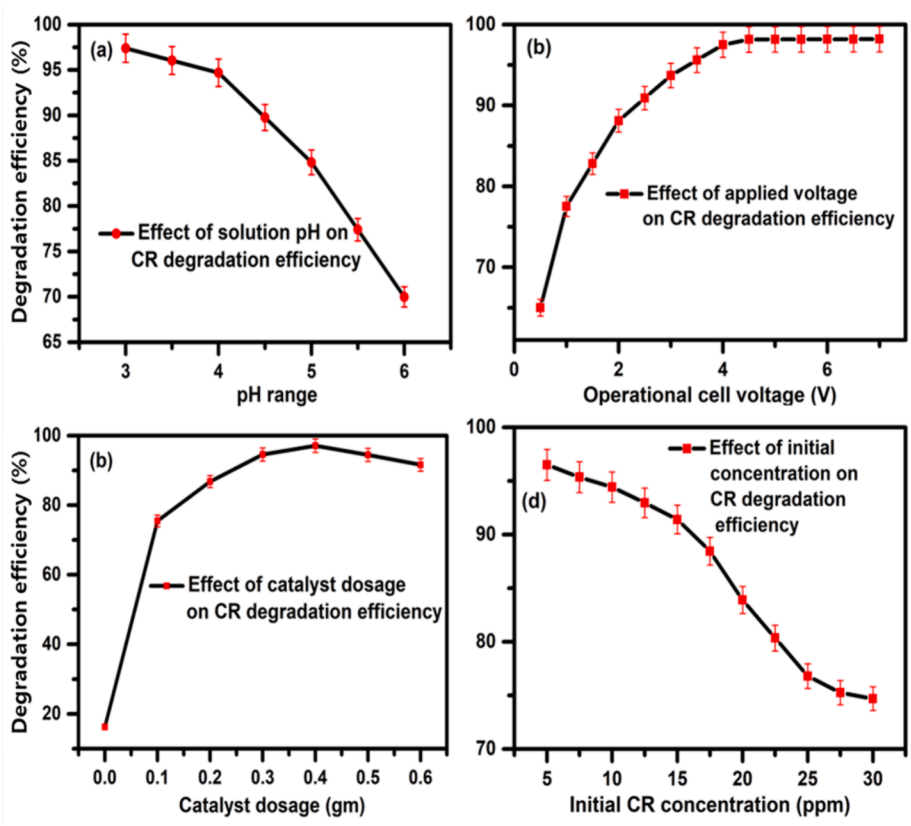

Fig. 6. Effects of pH (a), applied voltage (b), catalyst dosage (c), and initial CR-concentration (d) on CR-degradation. Na_2SO_4 of 0.5 mol L^{-1} is used as electrolyte.

recycling between Fe^{3+} and Fe^{2+} in the system, resulting in a higher degradation efficiency. However, when the applied potential was over 5.5 V, an insignificant increase of the CR removal rate (95 ± 2 to 98 ± 2 %) was observed. This might be associated with scavenging effects of Fe^{2+} and H_2O_2 for •OH-radicals generation (Menon et al., 2021; Zou et al., 2020). Consequently, applied voltage of 2.5 V was identified as the optimal voltage for subsequent experiments.

The performance of EF oxidation was also affected by catalyst dosage. The effect of the addition of MNPs as heterogeneous catalyst to the EF system for CR degradation was investigated. When 0.1 g of MNPs was added to the EF system with an ACF electrode, the CR removal efficiency dramatically increased to 86 ± 2 % compared to the non-

catalyzed system (15 ± 1.2 %) (Fig. 6c). With an additional dosage of heterogeneous catalyst (0.4 g of MNPs) to the system, the CR degradation efficiency further increased to 96 ± 2 %. More Fe^{2+} would trigger the rapid generation of H_2O_2 and subsequent •OH radicals on the cathode surface (Nordin et al., 2020). The role of homogenous Fe^{2+} ions in the system acted as a channel for electron transfer to pull off the H_2O_2 from the active sites of the ACF cathode. This pull system might contribute to the release of H_2O_2 in the system; then, H_2O_2 was allowed to react with Fe^{2+} ion to generate •OH radicals (Ergan and Gengec, 2020). However, additional increase of the MNPs dose to 0.5 or 0.6 g could not further improve the removal rate. It was hypothesized that Fe^{2+}, if added excessively, might also consume •OH radicals (i.e., inhibition effect). The result could also be due to the maximum limit of the active sites of the ACF for H_2O_2 generation. A similar result was also reported (Cui et al., 2021) in the Fenton process for CR degradation. From the analysis in this study 0.3 g MNPs dosage was enough to facilitate the heterogeneous EF CR degradation. The degradation of CR relied on the particle size and iron content of MNPs as confirmed by FESEM and EDX analysis (Boutemedjet et al., 2021). Similarly, smaller particles have a higher surface area to volume ratio, which contributed to higher degradation of CR through catalyst-CR molecule interaction.

Lastly, the effect of the initial CR concentration on the EF oxidation process was determined. When the initial CR concentration was increased while keeping the other parameters constant, the degradation efficiency declined (Sun et al., 2020). As the concentration of CR increased from 5 to 20 mg L^{-1}, the degradation efficiency was maintained above 94 ± 1.5 % over a 40 min. reaction time. However, the removal efficiency deteriorated when the CR concentration was increased to 30 mg L^{-1} (73 ± 2 % removal efficiency) as described in Fig. 6d. From the result, it was assumed that all the active sites of MNPs would be occupied if the initial CR concentration was extremely high, resulting in incomplete CR degradation. If it is the case, more MNPs should be added. The EF oxidation process having the operational parameters, which resulted in the CR removal efficiency of more than 90 %, was considered as the optimum concentration. Therefore, 15 mg L^{-1} was used as the initial CR concentration in the subsequent analysis.

3.5. Rate constant and dominant oxygen-reactive species

Using the measured current density (14.5 ± 1.23 mA cm^{-2}) and other constants n (78 e), F (96,485.3 C mol^{-1}), k_D (0.078 cm s^{-1}), A (8.75 cm^2), C^0 (15 mg L^{-1} CR), and V (300 cm^3), the apparent rate constant (k_{app}) at optimal parameters (pH value 4, voltage 2.5 V, and catalyst dose 0.3 g) was determined (Eqs. (11) and (12)). As a result, the EF-based CR degradation was governed by pseudo-second-order rate kinetics, with an approximate value of 8.78 × 10^{-4} ± 1.72 × 10^{-5} mol^{-1} cm^3 min^{-1} (0.878 ± 0.017 M^{-1} min^{-1}) rate constant.

To determine the superior free active species generated in the EF system, the process was applied for oxidizing 15-mg L^{-1} CR in the presence of alcohols and p-benzoquinone (p-BQ) to quench •OH and superoxide ion ($O_2^{\cdot-}$) radicals, respectively (Hussain et al., 2020). Excess concentration of scavenging chemicals was used to ensure a complete trapping of radials from the bulk solution in the system. As demonstrated in (Fig. S4a), the percentage CR removal declined sharply to 17 ± 1 % from 94 ± 2 % after the addition of an excess of ethanol concentration (0.25 mol L^{-1}) to the reactor. The 17 ± 1.2 % removal efficiency of CR could be attributed to a non-radical reaction mechanism such as singlet oxygen, which might be generated from the transfer of a single electron through the surface of ACF during the EF process (Guo et al., 2022). Similarly, an addition of excess concentration of tertiary butyl alcohol (TBA) (0.25 mol L^{-1}) to the reacting system, the degradation of CR declined to 28.5 % due to less inhibition effect of TBA on •OH radicals than that of EtOH. The EtOH and TBA quenching analysis indicated that •OH radicals played a crucial role in CR degradation in the EF system. The number of electrons transferred (2.16 ± 0.02 e) and the approximate H_2O_2 generated (90.0 ± 1.3) were checked in the presence of chemical quenching (Figs. S4b and S4c, respectively), indicating the system followed 2e-ORR. However, addition of 0.25 mol L^{-1} of p-BQ to the reacting system resulted in a slight change in the CR removal efficiency; 88 ± 2 % removal efficiency was obtained. This result clearly indicated that the role of $O_2^{\cdot-}$ ion radicals was not as significant as •OH. Instead, •OH radicals were found to be the superior free active oxygen species in this system. An insignificant amount of superoxide radicals might be formed via the reduction of oxygen on the cathodic surface according to Eqs. (18) or (19) and consumed for H_2O_2 formation in acidic bulk system (Eq. (20)). It was concluded that the dominant free reactive oxygen species generated in the EF system were •OH radicals.

$$O_2 + 2e^- \rightarrow O_2^{\cdot-} \quad (18)$$

$$Fe(II) + O_2 \rightarrow Fe(II) + O_2^{\cdot-} \quad (19)$$

$$O_2^{\cdot-} + 2H^+ \rightarrow H_2O_2 + O_2 \quad (20)$$

3.6. Mineralization efficiency and energy consumption

The extent of CR mineralization was measured based on the presence of the TOC in the treated solution. The values of TOC have been related to the total organic carbon of the CR solution. The TOC analysis at different time intervals indicated the degrees of mineralization (Ergan and Gengec, 2020). Performing at optimal operating parameters, a reasonable TOC removal of about 56 ± 2 % was observed over 40 min, while the color removal was 94 ± 2 %. However, when the reaction time was increased to 120 min, the mineralization efficiency could reach 83 ± 3 % with the complete color removal, confirming that the chromophore of CR, i.e., azo bond (–N═N–) would be easier to destroy than an aromatic ring (Fig. S5a). EF mineralization of high-molecular-weight dyes such as CR (MW-697 g mol^{-1}) over short-time reaction was not possible due to the confinement of quite-stable benzene ring molecules that could not break apart in the system.

The primary cost associated with the EF process is incurred by electricity and its consumption should be analyzed. The degradation rate of CR at different cell potential (0.5–6.5 V) was related to the energy consumption (kWh (g TOC)$^{-1}$) of the system (Ergan and Gengec, 2020; Menon et al., 2021). The main requirements for electrochemical advanced oxidation processes in breakdown of organic contaminants are high mineralization efficiency and low energy consumption. Here, an innovative and energy-efficient EF system was required to minimize the cost energy consumption. Within 40 min., a satisfactory CR mineralization (i.e., 57 ± 2 % TOC removal) could be achieved when the system was run at an applied potential of 2.5 V. increasing the applied voltage to 6.5 V, a 61 ± 3 % TOC removal was observed accounting to an increase of 4 % in TOC removal. At larger applied voltages, relatively higher mineralization efficiency was noted. However, when the applied voltage increased to 6.5 V, a small TOC removal enhancement was observed. It was noteworthy that when the applied voltage was increased from 2.5 V to 6.5 V, the TOC removal increased by 4 % only, but the energy consumption increased by 53 % (from 0.032 to 0.051 kWh (g TOC)$^{-1}$). The result indicates that it would not be cost-effective to achieve a higher mineralization efficiency at a higher applied voltage. Comparing the above applied voltages in terms of their energy consumption and CR mineralization efficiency, the latter (2.5 V) would be considered as the optimal applied voltage for CR mineralization. Therefore, the applied voltage of 2.5 V was an energy-efficient and cost-effective voltage to mineralize CR to approximately 83 ± 2 % over 120 min. While CR was degrading at an applied potential of 2.5 V, 14.5 ± 3 mA cm^{-2} current density was measured and the mineralization current density efficiency of about 58 ± 2 % was estimated.

3.7. Stability and reusability

Stability and reusability are another important parameters in evaluating the performance of the catalysis and electrodes (i.e., MNPs and ACF) which are evaluated by their repeated use in the EF oxidation. These parametric analyses were helpful in determining the extended loss of an active species of MNPs. The catalyst was isolated from the reacting medium of the CR degradation using an external magnet, which was repeated ten times. The quantity of dissolved iron in the reaction solution was determined via ICP-OES analysis. About 0.021 mg L^{-1} iron residuals were detected, indicating 98 % recovery, which is comparable to the amount of iron residual obtained in the first EF oxidation (i.e., negligible compared to 0.3 g of MNPs initially added. However, the CR degradation capability of the catalysts decreased significantly (from 94 ± 2 % to 52 ± 3 %) over ten cycles as shown in Fig. S5b. A negligible amount of iron residuals in the reacting solution indicated that the magnetic characteristics of the MNPs were not altered. Nevertheless, the XRD result showed the crystalline characteristic peaks of MNPs (after ten cycles) disappeared compared to the XRD result before use, as shown by XRD analysis in Fig. S6a (blue). Only the major characteristic peaks at 20.4°, 36.7°, and 63.3° that correspond to (1 1 1), (3 1 1), and (4 4 0) lattice planes (Cai et al., 2022) were observed, which indicate the MNPs crystal deformation. Although, the Fe-O vibrational mode with a smooth curve was observed at approximately 500–600 cm^{-1}, the FT-IR result of MNPs showed a deformed structure compared to the FT-IR result before used for EF oxidation (Fig. S6b, blue). Thus, the gradual decline of the CR degradation efficiency over ten cycles (54 ± 3 %) could be due to the deformation crystalline structure of MNPs. Despite their high degradation efficiency, iron-based catalysts have low reusability due to crystalline structural deformation (Zuo et al., 2021).

The amorphous nature of the ACF cathode was detected at 25.3° after several cycles of EF CR degradation (Rahmani et al., 2021) (Fig. S6b, red). The narrow peak of the ACF that was observed before degradation process were diminished, indicating that the crystal structure of the ACF was altered, and the active species (oxygen-containing functional groups) were eroded. Additionally, the FT-IR technique was employed to locate pertained functional groups on the ACF surface. The functional groups that were at 1655 cm^{-1} (–COOH) and 1554 cm^{-1} (–C═O) on ACF before the experiment disappeared as seen in Fig. S6b (red). The broad and loose absorption peaks of the material suggested that the surface-active groups were worn out through the degradation process. Similarly, the CV curve of ACF showed a −1.3 ± 0.36 mA cm^{-2} cathodic peak for 2e-ORR and a 0.9 ± 0.037 mA cm^{-2} anodic peak for water oxidation (Fig. S6c, red). The LSV analysis also showed 1.4 ± 0.25 mA cm^{-2} of water oxidation reaction on the system (Fig. S6d, red). The results indicated that the ACF cathode activity for 2e-ORR was declined and confirmed the structural change of the cathode (i.e., depletion of active oxygen-containing functional groups from the cathode surface). Thus, after ten cycles of CR degradation, 54 ± 3 % efficiency was observed over 40 min. under the optimal operating conditions. Generally, the strong reactive species generated gradually lowered the selectivity of ACF for 2e-ORR.

3.8. Degradation mechanisms and intermediate products

As aforementioned, CR could not be completely mineralized by the EF oxidation, although the CR color disappeared over 40 min. This indicated the destruction of the azo group (–N═N–) of CR and release of the intermediates formed by the •OH radicals attack (Cai et al., 2022). However, extending the reaction time to 120 min. contributed to the release of intermediate by-products. Eventually, the intermediates products were converted to inorganic ions through a continuous exposure to •OH radicals (Ergan and Gengec, 2020). To understand how the degradation mechanism and the possible degradation pathways of the intermediates in the system work, LC-MS and ICS techniques were employed. The degradation intermediates might be either aromatic with different substituents or aliphatic organic compounds (Fig. S7); thus, the possible and dominant reaction intermediate products of CR with their chemical structures are proposed in Fig. 7. Using LC-MS, the identified reaction products are listed along with their m/z values and molecular structures in Table S3. After 120 min. of CR degradation, 6.3 ± 0.17 mg L^{-1} NO_3^- concentration and 3.46 ± 0.1 mg L^{-1} SO_4^{2-} concentration were determined. About 83 ± 3 % of the nitrogen and sulfur atoms contained by CR were oxidized and released into bulk water as described in Fig. S8. The material balance calculations and experimental results of CR EF degradation are demonstrated in Table S4.

3.9. Oxidation assessment on dye-containing real wastewater

EF degradation assessment for different dye-containing wastewater was performed to confirm the potential application for real wastewater treatment (Chandanshive et al., 2020; Nakhate et al., 2020). We followed similar procedures and mechanisms to the CR degradation as mentioned above, where we used two stacks of ACF-SS-ACF in which ACF and SS were used as the cathode and anode, respectively (Figs. S9a and S9b). In the real textile wastewater oxidation assessment, the effective working volume of the reactor was 300 mL and adjusted to pH value of 4. The reactor was employed with the applied voltage of 2.5 V, catalyst dosage of 0.3 g, and the total dye concentration of 45 mg L^{-1} at optimum operating conditions. As demonstrated in Figs. S10a and S10b, the initial concentration of individual dyes and the mixture of the wastewater was analyzed at their maximum absorbance. However, while mixing with real wastewater, the absorbance peak of each dye was not clear compared to the individual absorbance peaks. This could be due to the shielding effect of the wastewater matrix on the chromophores of dyes. After 120 min. of EF degradation, 3 mL of samples were harvested and filtered for UV–Vis, TOC, LC-Ms, and IC analysis. As shown in Fig. S10c, the UV–Vis of absorption peaks of each dye diminished, indicating that the chromophore bonds were broken apart, and the maximum degradation efficiency for CR, MB, and AO II were calculated to be 72 ± 2 %, 82 ± 2 %, and 93 ± 2 %, respectively (Cai et al., 2022; de Oliveira Guidolin et al., 2021). The detection of high concentrations of inorganic ions (NO_3^- and SO_4^{2-}) in the IC analysis and decreasing the TOC concentration confirmed the mixture of the wastewater was degraded into inorganic compounds CO_2 and H_2O. The measured values of the dye-containing wastewater are described in Table S5. The overall CR oxidation and dye-containing real wastewater decontamination confirmed that the proposed EF oxidation system was capable of degrading and mineralizing a complex matrix of real wastewater.

4. Conclusion

In accordance with the soaking principle, active functional groups such as carboxyl (–C═O-OH), carbonyl (–C═O), hydroxyl (–OH), and nitrous (–N–O) were generated on the surface of ACF. Using size-controlled MNP catalysts, EF oxidation of CR-containing wastewater was conducted using an ACF cathode. The oxygen-containing functional groups served as sites for H_2O_2 generation, and the heterogeneous Fe^{2+} acted as a driving force to detach the H_2O_2 from the site to generate •OH radicals. An approximate 89 ± 3 % of H_2O_2 generation was determined following the 2e-ORR mechanism. Using the model contaminant (CR), degradation efficiency of >94 % and mineralization efficiency of >82 % were obtained in 40 min and in 120 min, respectively. Finally, the oxidation system was applied for treating dye-containing real wastewater. Over 2 h of EF oxidation, the removal efficiency of the system to a mixture of wastewater of CR, MB, and AO II were calculated to be 72 ± 2 %, 82 ± 2 %, and 93 ± 2 %, respectively. These satisfactory results of EF oxidation indicated that the system could be applied for treating industrial wastewater.

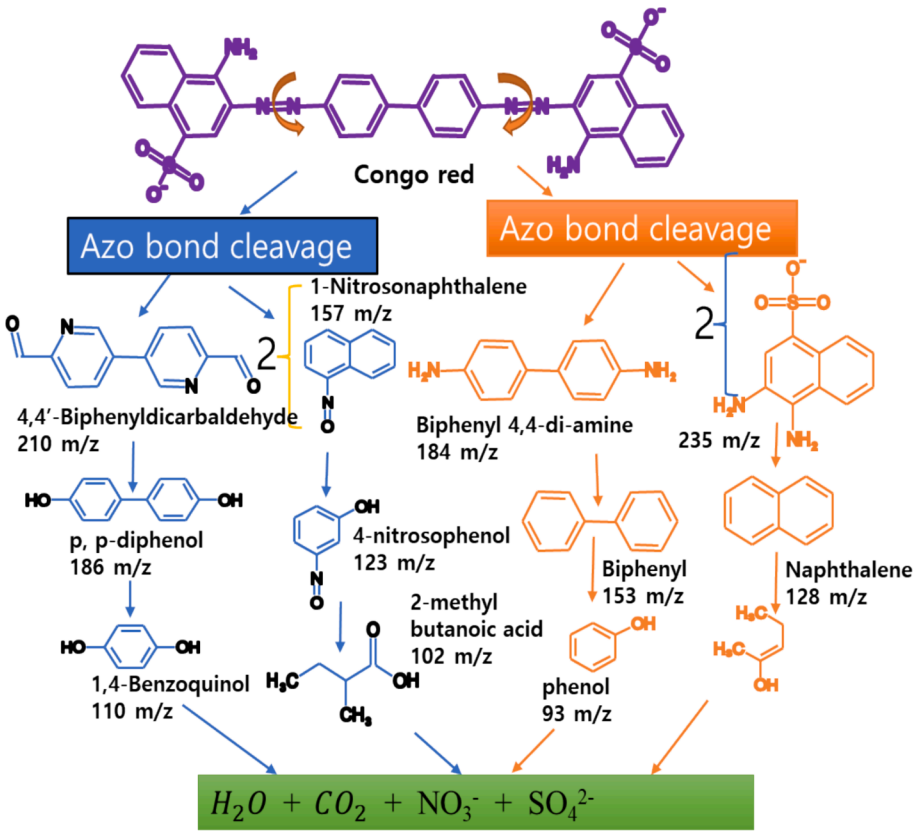

Fig. 7. Possible fate of CR degradation using an ACF cathode in the EF process, at optimal operating conditions (pH, 4), applied potential (2.5 V), catalyst dose (0.3 g), initial CR concentration (15 mg L^{-1}), and electrolyte (Na_2SO_4, 0.5 mol L^{-1}) and 120 min.

CRediT authorship contribution statement

Redae Nuguse Berhe: Formal analysis, Data curation, Conceptualization. **Monu Verma:** Writing – review & editing. **Cong Li:** . **Shimelis Kebede Kassahun:** Supervision. **Joon Wun Kang:** . **Hyunook Kim:** Supervision, Writing – review & editing.

Declaration of competing interest

The authors declare that they have no known competing financial interests or personal relationships that could have appeared to influence the work reported in this paper.

Data availability

Data will be made available on request.

Acknowledgments

H. Kim was supported by the Korea Environment Industry & Technology Institute (KEITI) through Development of Demonstration Technology for Converting Unconventional Waste Biomass to Energy funded by the Korea Ministry of Environment (MOE) (Grant No. 2022003480001) and KEITI through Post Plastic, a specialized program of the Graduate School funded by the MOE.

Appendix A. Supplementary data

Supplementary data to this article can be found online at https://doi.org/10.1016/j.ces.2024.120711.

References

Bello, M.M., Abdul Raman, A.A., Asghar, A., 2019. A review on approaches for addressing the limitations of Fenton oxidation for recalcitrant wastewater treatment. Process Saf. Environ. Prot. 126, 119–140. https://doi.org/10.1016/j.psep.2019.03.028.

Berhe, R.N., Kassahun, S.K., Kang, J.W., Verma, M., Kim, H., 2022. Synthesis of Fe3O4/CNT/ACF cathode-based electro-fenton system for efficient mineralization of Methylene blue dye: kinetics and mechanism. J. Environ. Chem. Eng. 10 (6), 108672 https://doi.org/10.1016/j.jece.2022.108672.

Berhe, R.N., Kassahun, S.K., Kang, J.W., Lee, I., Verma, M., Kim, H., 2023. Performance evaluation of Fe3O4@ACF-supported bio-electro Fenton system for simultaneous sewage treatment and methyl orange degradation. Mater. Today Commun. 35 (April), 106331 https://doi.org/10.1016/j.mtcomm.2023.106331.

Boutemedjet, A., Djerad, S., Tifouti, L., Bachari, K., 2021. Effect of Fe0 content on the effectiveness of Fe0/Fe3O4 catalyst in Fenton process. J. Water Process Eng. 41 (March), 102079 https://doi.org/10.1016/j.jwpe.2021.102079.

Cai, H., J. Zou, J. Lin, J. Li, Y. Huang, S. Zhang, B. Yuan, J. Ma, 2022. Sodium hydroxide-enhanced acetaminophen elimination in heat/peroxymonosulfate system: Production of singlet oxygen and hydroxyl radical, Chem. Eng. J., 429 (September 2021): 132438. Doi: 10.1016/j.cej.2021.132438.

Chandanshive, V., Kadam, S., Rane, N., Jeon, B.H., Jadhav, J., Govindwar, S., 2020. In situ textile wastewater treatment in high rate transpiration system furrows planted with aquatic macrophytes and floating phytobeds. Chemosphere 252, 126513. https://doi.org/10.1016/j.chemosphere.2020.126513.

Chen, D.R., Adusei, P.K., Chitranshi, M., Fang, Y., Johnson, K., Schulz, M., Shanov, V., 2021. Electrochemical activation to enhance the volumetric performance of carbon nanotube electrodes. Appl. Surf. Sci. 541 (July 2020), 148448 https://doi.org/10.1016/j.apsusc.2020.148448.

Cui, X., Zhang, S.-S., Gen, Y., Zhen, J., Zhan, J., Cao, C., Ni, S.-Q., 2021. Synergistic catalysis by Fe3O4-biochar/peroxymonosulfate system for the removal of bisphenol a. Sep. Purif. Technol. 276 (July), 119351 https://doi.org/10.1016/j.seppur.2021.119351.

Dash, A., Ahmed, M.T., Selvaraj, R., 2019. Mesoporous magnetite nanoparticles synthesis using the Peltophorum pterocarpum pod extract, their antibacterial efficacy against pathogens and ability to remove a pollutant dye. J. Mol. Struct. 1178, 268–273. https://doi.org/10.1016/j.molstruc.2018.10.042.

de Oliveira Guidolin, T., N. M. Possolli, M. B. Polla, T. B. Wermuth, T. Franco de Oliveira, S. Eller, O. R. Klegues Montedo, S. Arcaro, and M. A. P. Cechinel, 2021. "Photocatalytic pathway on the degradation of methylene blue from aqueous solutions using magnetite nanoparticles." *J. Clean. Prod.*, 318 (March). Doi: 10.1016/j.jclepro.2021.128556.

Ergan, B.T., Gengec, E., 2020. Dye degradation and kinetics of online Electro-Fenton system with thermally activated carbon fiber cathodes. J. Environ. Chem. Eng. 8 (5), 104217 https://doi.org/10.1016/j.jece.2020.104217.

Gang, Q., Niaz Akhtar, M., Boudaghi, R., 2021. Development of high-efficient double layer microwave absorber based on Fe3O4/carbon fiber and Fe3O4/rGO. J. Magn. Magn. Mater. 537 (April), 168181 https://doi.org/10.1016/j.jmmm.2021.168181.

Gao, Y., Zhu, W., Wang, C., Zhao, X., Shu, M., Zhang, J., Bai, H., 2020. Enhancement of oxygen reduction on a newly fabricated cathode and its application in the electro-Fenton process. Electrochim. Acta 330, 135206. https://doi.org/10.1016/j.electacta.2019.135206.

Gao, Y., Zhu, W., Li, Y., Li, J., Yun, S., Huang, T., 2021. Novel porous carbon felt cathode modified by cyclic voltammetric electrodeposited polypyrrole and anthraquinone 2-sulfonate for an efficient electro-Fenton process. Int. J. Hydrogen Energy 46 (15), 9707–9717. https://doi.org/10.1016/j.ijhydene.2020.04.197.

Greczynski, G., Hultman, L., 2020. X-ray photoelectron spectroscopy: Towards reliable binding energy referencing. Prog. Mater. Sci. 107 (April 2019), 100591 https://doi.org/10.1016/j.pmatsci.2019.100591.

Guo, Y., Long, J., Huang, J., Yu, G., Wang, Y., 2022. Can the commonly used quenching method really evaluate the role of reactive oxygen species in pollutant abatement during catalytic ozonation? Water Res. 215 (December 2021) https://doi.org/10.1016/j.watres.2022.118275.

Hachemaoui, M., Mokhtar, A., Mekki, A., Zaoui, F., Abdelkrim, S., Hacini, S., Boukoussa, B., 2020. International Journal of Biological Macromolecules Composites beads based on Fe 3 O 4 @ MCM-41 and calcium alginate for enhanced catalytic reduction of organic dyes. Int. J. Biol. Macromol. 164, 468–479. https://doi.org/10.1016/j.ijbiomac.2020.07.128.

Hassan, A., Tzedakis, T., 2020. Facile chemical activation of graphite felt by KMnO4 acidic solution for vanadium redox flow batteries. Appl. Surf. Sci. 528 (June), 146808 https://doi.org/10.1016/j.apsusc.2020.146808.

Hong, Y., Oh, J., Lee, I., Fan, C., Pan, S.Y., Jang, M., Park, Y.K., Kim, H., 2021. Total-organic-carbon-based quantitative estimation of microplastics in sewage. Chem. Eng. J. 423 (December 2020), 130182 https://doi.org/10.1016/j.cej.2021.130182.

Hu, Q., Dong, Y., Ma, K., Meng, X., Ding, Y., 2022. Amidation crosslinking of polymeric carbon nitride for boosting photocatalytic hydrogen peroxide production. J. Catal. 413, 321–330. https://doi.org/10.1016/j.jcat.2022.06.042.

Huong Le, T.X., Bechelany, X.M., Cretin, M., 2017. Carbon felt based-electrodes for energy and environmental applications: A review. Carbon N. Y. 122, 564–591. https://doi.org/10.1016/j.carbon.2017.06.078.

Hussain, S., E. Aneggi, S. Briguglio, M. Mattiussi, V. Gelao, I. Cabras, L. Zorzenon, A. Trovarelli, D. Goi, 2020. Enhanced ibuprofen removal by heterogeneous-Fenton process over Cu / ZrO 2 and Fe / ZrO 2 catalysts, J Environ. Chem. Eng. 8 (November 2019). 10.1016/j.jece.2019.103586.

Jafari, M., Hasanzadeh, I., Jafari Eskandari, M., Hasanzadeh, I., 2021. Size-controlled synthesis of Fe3O4 magnetic nanoparticles via an alternating magnetic field and ultrasonic-assisted chemical co-precipitation. Mater. Sci. Eng. B Solid-State Mater. Adv. Technol. 266 (February), 115050 https://doi.org/10.1016/j.mseb.2021.115050.

Jang, C.R., Ji, J.M., Yu, J.H., 2021. Applicability of CNT as support candidate for thiophene hydrodesulfurization and 1-octene hydrogenation catalyst. Inorg. Chem. Commun. 129 (March), 108615 https://doi.org/10.1016/j.inoche.2021.108615.

Jiang, S., Qian, K., Yu, K., Zhou, H., Weng, Y., Zhang, Z., 2021. Study on ultralight and flexible Fe3O4/melamine derived carbon foam composites for high-efficiency microwave absorption. Chem. Phys. Lett. 779 (April), 138873 https://doi.org/10.1016/j.cplett.2021.138873.

Kim, J.H., Kim, S.H., Kim, B.J., Lee, H.M., 2023. Effects of oxygen-containing functional groups on the electrochemical performance of activated carbon for EDLCs. Nanomaterials 13 (2). https://doi.org/10.3390/nano13020262.

Kim, M., Song, Y.E., Xiong, J.Q., Kim, K.Y., Jang, M., Jeon, B.H., Kim, J.R., 2021. Electrochemical detection and simultaneous removal of endocrine disruptor, bisphenol A using a carbon felt electrode. J. Electroanal. Chem. 880, 114907 https://doi.org/10.1016/j.jelechem.2020.114907.

Li, X., Xiao, C., Ruan, X., Hu, Y., Zhang, C., Cheng, J., Chen, Y., 2021. Enrofloxacin degradation in a heterogeneous electro-Fenton system using a tri-metal-carbon nanofibers composite cathode. Chem. Eng. J. 427 (June 2021) https://doi.org/10.1016/j.cej.2021.130927.

Liu, X., Lu, J., Fang, X., Zhou, J., Chen, Q., 2022. Complexation modelling and oxidation mechanism of organic pollutants in cotton pulp black liquor during iron salt precipitation and electrochemical treatment. Chemosphere 308 (P2), 136374. https://doi.org/10.1016/j.chemosphere.2022.136374.

Liu, H., Zhang, Y., Zhou, Y., Chen, Z., Lichtfouse, E., 2020. Self-provided microbial electricity enhanced wastewater treatment using carbon felt anode coated with amino-functionalized Fe3O4. J. Water Process Eng. 38 (August), 101649 https://doi.org/10.1016/j.jwpe.2020.101649.

Magro, M., Molinari, S., Venerando, A., Baratella, D., Zoppellaro, G., Salviulo, G., Zboril, R., Vianello, F., 2020. Colloidal maghemite nanoparticles with oxyhydroxide-like interface and chiroptical properties. Appl. Surf. Sci. 534 (August), 147567 https://doi.org/10.1016/j.apsusc.2020.147567.

Medina-ramírez, I.E., C.E.D. De León-macias, G. Pedroza-herrera, R. Gonzáles-segovia, J. Antonio, J.L. Rodríguez-lópez, 2019. Evaluation of the biocompatibility and growth inhibition of bacterial bio films by ZnO, Fe3O4 and ZnO @ Fe 3O4 photocatalytic magnetic materials, Ceram. Int., (December): 0–1. Doi: 10.1016/j.ceramint.2019.12.145.

Mehdizadeh, P., Masjedi-Arani, M., Amiri, O., Salavati-Niasari, M., 2021. Rapid microwave fabrication of new nanocomposites based on Tb-Fe-O nanostructures for electrochemical hydrogen storage application. Fuel 304 (June), 121412. https://doi.org/10.1016/j.fuel.2021.121412.

Menon, P., Anantha Singh, T.S., Pani, N., Nidheesh, P.V., 2021. Electro-Fenton assisted sonication for removal of ammoniacal nitrogen and organic matter from dye intermediate industrial wastewater. Chemosphere 269, 128739. https://doi.org/10.1016/j.chemosphere.2020.128739.

Nakhate, P.H., Moradiya, K.K., Patil, H.G., Marathe, K.V., Yadav, G.D., 2020. Case study on sustainability of textile wastewater treatment plant based on lifecycle assessment approach. J. Clean. Prod. 245, 118929 https://doi.org/10.1016/j.jclepro.2019.118929.

Nordin, N., Ho, L., Ong, S., Haqi, A., Latif, A., Rani, A., Lee, S., Ong, Y., 2020. Chemosphere Hydroxyl radical formation in the hybrid system of photocatalytic fuel cell and peroxi-coagulation process affected by iron plate and UV light. Chemosphere 244, 125459. https://doi.org/10.1016/j.chemosphere.2019.125459.

Perecin, C. J., B. M. Tirich, L. C. C. M. Nagamine, G. Porto, F. V. Rocha, N. N. P. Cerize, and L. C. Varanda, 2021. "Aqueous synthesis of magnetite nanoparticles for magnetic hyperthermia: Formation mechanism approach, high water-dispersity and stability." *Colloids Surfaces A Physicochem. Eng. Asp.*, 627 (July). Doi: 10.1016/j.colsurfa.2021.127169.

Qian, W.M., Vahid, M.H., Sun, Y.L., Heidari, A., Barbaz-Isfahani, R., Saber-Samandari, S., Khandan, A., Toghraie, D., 2021. Investigation on the effect of functionalization of single-walled carbon nanotubes on the mechanical properties of epoxy glass composites: Experimental and molecular dynamics simulation. J. Mater. Res. Technol. 12, 1931–1945. https://doi.org/10.1016/j.jmrt.2021.03.104.

Rahmani, A., Seid-mohammadi, A., Leili, M., Shabanloo, A., Ansari, A., Alizadeh, S., Nematollahi, D., 2021. Electrocatalytic degradation of diuron herbicide using three-dimensional carbon felt/β-PbO2 anode as a highly porous electrode: Influencing factors and degradation mechanisms. Chemosphere 276, 130141. https://doi.org/10.1016/j.chemosphere.2021.130141.

Sheikhmohammadi, A., Asgari, E., Nourmoradi, H., Fazli, M.M., Yeganeh, M., 2021. Ultrasound-assisted decomposition of metronidazole by synthesized TiO2/Fe3O4 nanocatalyst: Influencing factors and mechanisms. J. Environ. Chem. Eng. 9 (5), 105844 https://doi.org/10.1016/j.jece.2021.105844.

Sun, F., Liu, H., Wang, H., Shu, D., Chen, T., Zou, X., Huang, F., Chen, D., 2020. Science of the Total Environment A novel discovery of a heterogeneous Fenton-like system based on natural siderite : A wide range of pH values from 3 to 9. Sci. Total Environ. 698, 134293 https://doi.org/10.1016/j.scitotenv.2019.134293.

Wu, S., Sun, A., Zhai, F., Wang, J., Xu, W., Zhang, Q., Volinsky, A.A., 2011. Fe3O4 magnetic nanoparticles synthesis from tailings by ultrasonic chemical co-precipitation. Mater. Lett. 65 (12), 1882–1884. https://doi.org/10.1016/j.matlet.2011.03.065.

Xia, Y., Shang, H., Zhang, Q., Zhou, Y., Hu, X., 2019. Electrogeneration of hydrogen peroxide using phosphorus-doped carbon nanotubes gas diffusion electrodes and its application in electro-Fenton. J. Electroanal. Chem. 840 (February), 400–408. https://doi.org/10.1016/j.jelechem.2019.04.009.

Xing, X., Liu, R., Anjass, M., Cao, K., Kaiser, U., Zhang, G., Streb, C., 2020. Bimetallic manganese-vanadium functionalized N, S-doped carbon nanotubes as efficient oxygen evolution and oxygen reduction electrocatalysts. Appl. Catal. B Environ. 277 (February), 119195 https://doi.org/10.1016/j.apcatb.2020.119195.

Xu, F., Cui, Y., Bao, D., Lin, D., Yuan, S., Wang, X., Wang, H., Sun, Y., 2020. A 3D interconnected Cu network supported by carbon felt skeleton for highly thermally conductive epoxy composites. Chem. Eng. J. 388 (December 2019) https://doi.org/10.1016/j.cej.2020.124287.

Xu, Y., Guo, D., Luo, Y., Xu, J., Guo, K., Wang, W., Liu, G., Wu, N., Liu, X., Qin, A., 2023. Constructing abundant oxygen-containing functional groups in hard carbon derived from anthracite for high-performance sodium-ion batteries. Nanomaterials 13 (23). https://doi.org/10.3390/nano13233002.

Yao, B., Luo, Z., Yang, J., Zhi, D., Zhou, Y., 2021. FeIIFeIII layered double hydroxide modified carbon felt cathode for removal of ciprofloxacin in electro-Fenton process. Environ. Res. 197 (March), 111144 https://doi.org/10.1016/j.envres.2021.111144.

Zanchettin, G., G. da S. Falk, S. Y. G. González, D. Hotza, 2021. "High performance magnetically recoverable Fe3O4 nanocatalysts: fast microwave synthesis and photo-fenton catalysis under visible-light." Chem. Eng. Process. - Process Intensif., 166 (April). Doi: 10.1016/j.cep.2021.108438.

Zhang, J., Qiu, S., Feng, H., Hu, T., Wu, Y., Luo, T., Tang, W., Wang, D., 2022. Efficient degradation of tetracycline using core–shell Fe@Fe2O3-CeO2 composite as novel heterogeneous electro-Fenton catalyst. Chem. Eng. J. 428 (2021), 1–10. https://doi.org/10.1016/j.cej.2021.131403.

Zou, R., Angelidaki, I., Yang, X., Tang, K., Andersen, H.R., Zhang, Y., 2020. Degradation of pharmaceuticals from wastewater in a 20-L continuous flow bio-electro-Fenton (BEF) system. Sci. Total Environ. 727, 138684 https://doi.org/10.1016/j.scitotenv.2020.138684.

Zuo, M., Yi, S., Choi, J., 2021. Excellent dye degradation performance of FeSiBP amorphous alloys by Fenton-like process. J. Environ. Sci. (China) 105, 116–127. https://doi.org/10.1016/j.jes.2020.12.032.